J Therm Anal Calorim (2010) 99:957–963
DOI 10.1007/s10973-009-0643-x

Thermal stability of metastable nano-composites in planar flow cast Ti–Zr–Ni alloys

Emília Illeková · Helene Lefaix · Frederic Prima · Dušan Janičkovič · Peter Švec

MEDICTA2009 Special Issue

Abstract The influence of the solidification rate, the thermal stability, and devitrification process of the rapidly solidified $Ti_{45}Zr_{38}Ni_{17}$ alloy have been examined on ribbons prepared by the planar flow casting method. Differential scanning calorimetry in the continuous heating mode, X-ray diffraction, and electron microscopy techniques were applied. Comparison of the so-obtained microstructures revealed the competition between icosahedral quasicrystalline and β-Ti(Zr) phases, both dispersed in an amorphous matrix. It has been found that the decomposition process of rapidly quenched ribbons consists of the sequence of several independent exothermic and endothermic reactions involving the additional precipitation of quasi-crystalline nanoparticles and both irreversible and reversible changes between the unstable high-temperature β and stable low-temperature α phases. The formation of the intermetallics as well as the transformation of quasi-crystals into Laves phase has been observed at higher temperatures in all ribbons.

Keywords Amorphous phase · Kinetics · Quasi-crystals · Rapid solidification · Thermal stability · Ti–Zr–Ni alloy

E. Illeková (✉) · D. Janičkovič · P. Švec
Institute of Physics, Slovak Academy of Sciences, Dúbravská cesta 9, 845 11 Bratislava, Slovak Republic
e-mail: emilia.illekova@savba.sk; fyziille@savba.sk

H. Lefaix · F. Prima
Ecole Nationale Supérieure de Chimie de Paris, UMR CNRS 7045 Laboratoire de Métallurgie Strucurale, 11 rue Pierre et Marie Curie, 75231 Paris Cedex 05, France

Introduction

Among lightweight alloys, Ti-based materials appear as one of the most challenging systems for high-technological applications since they display an excellent corrosion resistance associated with outstanding mechanical characteristics. Nevertheless, their poor tribological properties generally result in industrial limitations. Rapid solidification methods, leading to new nano-composites microstructures, are shown to be an alternative elaboration way to overcome these drawbacks. The ternary Ti–Zr–Ni alloys are promising, considering their quasi-crystalline forming ability [1, 2] since quasi-crystalline materials are known to display peculiar properties (high hardness, low-surface energy, good tribological properties). Very recently, we highlighted the possibility to control the precipitation of crystalline phase as well as of quasi-crystals in $Ti_{45}Zr_{38}Ni_{17}$ by adapting processing parameters and as-quenched microstructures have been carefully investigated as a function of various processing parameters such as solidification rate or temperature of the melt [3, 4]. However, such microstructures are retained at room temperature in a very metastable state and undergo complex and multiple phase transformations upon thermal treatments. In this study, thermal stability and devitrification processes of planar flow cast ribbons are critically assessed using DSC investigation and the activation energies have been determined for all thermal transformations identified.

Experimental

The ingot of the $Ti_{45}Zr_{38}Ni_{17}$ master alloy was prepared by arc melting and four times re-melting of the 99.9% pure metals in an argon gas atmosphere. The 6-mm width ×

25-μm thickness solidified ribbons have been obtained by the planar flow casting of the melt on a rotating wheel. Various quenching temperatures $T_q > 1400$ K and quenching wheel speeds $f > 30$ m s^{-1} were used for the preparation of the individual samples so that the quenching rate was always higher than 10^6 K s^{-1}. The specific technological parameters T_q and f for four individual samples and the technological code characterizing each sample are summarized in Table 1. The true composition of the as-quenched ribbons did not differ from the nominal one by more than 1 at.%.

The differential scanning calorimetry (DSC) measurements were done in Perkin-Elmer DSC7 in the flowing argon atmosphere (20 mL min^{-1}) in the platinum sample pans with the platinum lids. The continuous heating mode and the heating rates of 5, 10, 20, 30, 40, and 60 K min^{-1} were used. The activation energies, E^*, of eventual phase transformations were calculated from the relation between the temperatures of the minima (or eventually maxima) of the transformation peaks, T_p, and the applied heating rates, Φ, following the Kissinger relation [5]. Following Elder [6,] the pre-exponential factors A could also be calculated from the same relation, namely

$$\ln\left(\Phi/T_p^2\right) = +\ln[(AR)/E^*] + \ln\Psi - E^*/\left(RT_p\right),$$

where R is the universal gas constant and the dimensionless function ln Ψ has been approximated (−0.0485) for the heating rates used in this article.

Table 1 Quenching temperature T_q, quenching wheel speed f, XRD characterization of the initial state, peak temperatures T_{pi}, transformation enthalpies ΔH_i, activation energies E_i^*, and pre-exponential factors A_i of the individual transformation steps, i, for the $Ti_{45}Zr_{38}Ni_{17}$ ribbons prepared by different technological parameters

Sample	M1520	M1521	M1522	M1576
T_q/K	1723	1693	1643	1423
f/m s^{-1}	40	40	40	36
Initial state	β in A	β in A	β in A	IQ in A
ΔH_{total}/J g^{-1}	−102	−104	−131	−77
T_{p1}/K	653.7	673.4	669.7	649.9
ΔH_{0+1}/%	70.4	58.2	64.3	61.9
E_1^*/kJ mol^{-1}	107 ± 5	182 ± 13	182 ± 13	117 ± 10
A_1/s^{-1}	5.56E+6	8.06E+12	5.57E+12	5.07E+7
$T_{p2'}$/K	No	872.0	No	859.0
$\Delta H_{2'}$/%	No	8.1	No	19.9
E_2^*/kJ mol^{-1}	–	379 ± 15	–	331 ± 18
$A_{2'}$/s^{-1}	–	2.49E+21	–	5.62E+18
$T_{p2''}$/K	No	No	No	No
$\Delta H_{2''}$/J g^{-1}	No	No	No	No
Tp_{endo}/K	No	894.1	894.1	No
ΔH_{endo}/J g^{-1}	No	7.8	6.5	No
E_{endo}^*/kJ mol^{-1}	–	392 ± 33	472 ± 18	–
A_{endo}/s^{-1}	–	4.26E+21	5.16E+26	–

The DSC heating rate is 40 K min^{-1}. β bcc Ti(Zr) with the lattice parameter $a_\beta = 0.343$ nm, A amorphous matrix, IQ icosahedral quasicrystals with $a_{IQ} = 0.513$ nm

For interpretations, the measurements with the empty pans forming the baseline and the subtraction method have been applied. The instrument was calibrated for all heating rates, the precision of measurements of temperature and the transformation heat is ±0.5 K, ±2 J g^{-1}.

The as-quenched as well as isothermally annealed ribbons were structurally characterized by X-ray diffraction (XRD) patterns and transmission electron microscopy (TEM). XRD measurements were performed in Bragg–Brentano geometry using CuKα radiation with a graphite monochromator in the diffracted beam. The lattice parameters were calculated from the angular positions of all available XRD peaks by linear extrapolation using least squares fitting as well as by total pattern analysis with the accuracy better than ±0.0003 nm. TEM observations were performed in a JEOL-2000FX microscope using samples polished by ion beam milling in a Gatan PIPS.

Results

Rapid solidification has been carried out on $Ti_{45}Zr_{38}Ni_{17}$ samples using planar flow casting method and various processing parameters reported in Table 1. The main parameter we focused on in this study is the quenching temperature T_q (the melt temperature before quench) influencing the solidification rate. As shown in previous study [3], rapid solidification of the $Ti_{45}Zr_{38}Ni_{17}$ alloy results in a composite structure composed by an amorphous (A) matrix containing a dispersion of bcc-Ti(Zr) (β phase) nanocrystalline particles having a size between 20 and 100 nm. We can notice that the initial volume fraction of nanocrystalline beta particles seems to depend on the quenching temperature, T_q, with a rather lower volume fraction for higher temperatures (see Fig. 1). DSC has been used to investigate the thermal stability of such composites structures, highlighting multiple phase transformation sequences.

In [3], the sample manifested three distinct exothermic DSC peaks by continuous heating up to 900 K, indicating that the decomposition of the duplex structure (A + β) takes place through three steps. The amorphous matrix relaxation and ω_{iso} precipitation in the as-quenched β particles was attributed to the first step. The formation of the nanometric icosahedral quasi-crystals (IQ) from the amorphous matrix being the main part of the devitrification process proceeded during the second, massive, exothermic transformation step. At higher temperatures, the third DSC effect was attributed to the precipitation of $(TiZr)_2Ni$

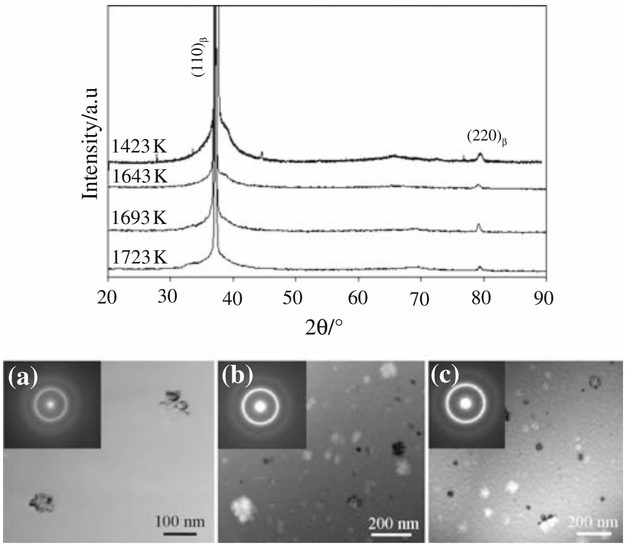

Fig. 1 Relation between the quenching temperature and the density of β-phase in the as-quenched $Ti_{45}Ar_{38}Ni_{17}$ ribbons. **a** Sample M1520, $T_q = 1723$ K. **b** Sample M1522, $T_q = 1643$ K. **c** Another sample, $T_q = 1423$ K

intermetallic phase and the growth of IQs. Further at temperatures above 900 K, the XRD patterns shoved the creation of the C14 hexagonal Laves phase and probably also the stable low-temperature hexagonal Ti(Zr) solid solution (α).

Our new results show that a typical DSC curve of the $Ti_{45}Zr_{38}Ni_{17}$ ribbon (see Fig. 2 for the sample M1521) should show four distinct irreversible exothermic events: namely the R0 exothermic pre-peak, the main devitrification exotherm R1, the R2′ exotherm, and upon heating to higher temperatures, the R2″ exotherm, or also another exothermal effect Rexo which might be between R1 and R2′ peaks.

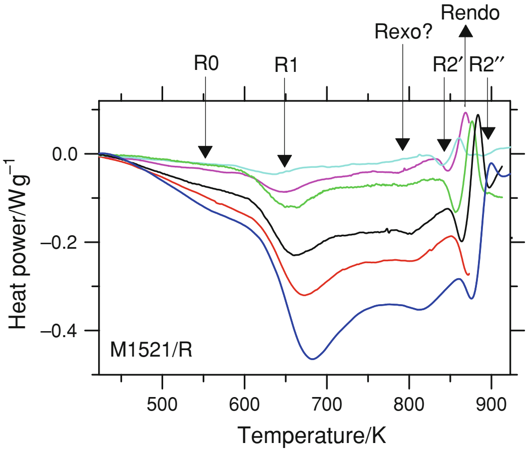

Fig. 2 The DSC curves of the ribbon $Ti_{45}Zr_{38}Ni_{17}$/M1521 for various heating rates from 5 to 60 K min^{-1}

Furthermore, varying the heating rate, we discovered an endothermic event Rendo which should be located at temperatures between R2′ and R2″ exothermic events (see, e.g., Fig. 2, the DSC curve for the heating rate 30 °C min^{-1}).

Modifying the technological parameters, meaning the solidification rate, we were able to prepare ribbons with variable proportion between the high-temperature exothermic and endothermic events. Namely, the sample M1520 (Fig. 3) does not show neither R2′ or R2″ exothermic peaks nor the Rendo effect, the sample M1522 (Fig. 4) has only the Rendo peak and no R2′ or R2″ exotherms, whereas the sample M1576 (Fig. 5) manifests no endotherm but only a single exothermic effect in the temperature range 823–923 K. In addition, the enthalpy of the first large exotherm R1, ΔH_1, being the main part of the total exothermic effect, ΔH_{total}, is evidently proportional to the solidification rate; namely, it increases increasing T_q and also f (see Table 1). The XRD and TEM results in

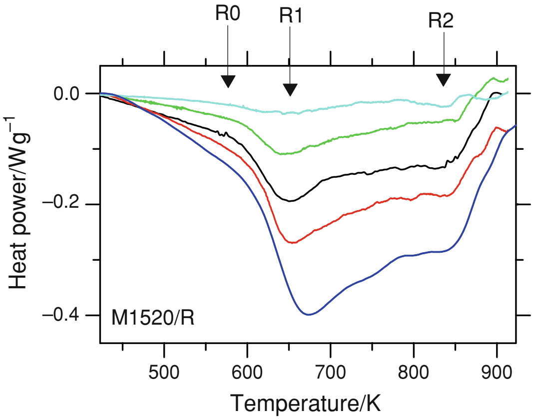

Fig. 3 The DSC curves of the ribbon $Ti_{45}Zr_{38}Ni_{17}$/M1520 for various heating rates from 5 to 60 K min^{-1}

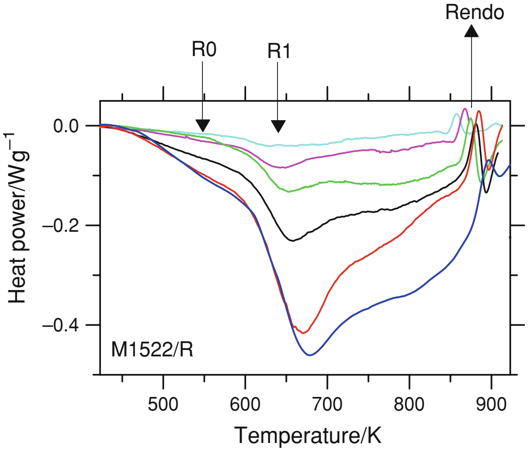

Fig. 4 The DSC curves of the ribbon $Ti_{45}Zr_{38}Ni_{17}$/M1522 for various heating rates from 5 to 60 K min^{-1}

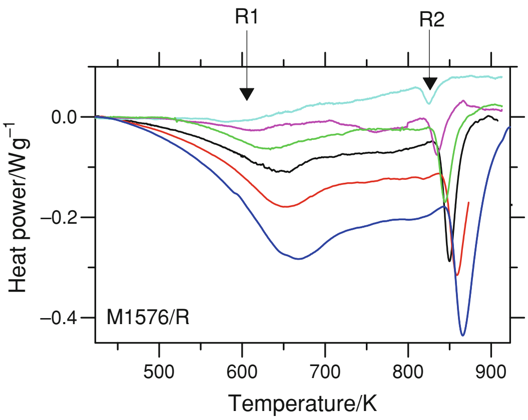

Fig. 5 The DSC curves of the ribbon $Ti_{45}Zr_{38}Ni_{17}$/M1576 for various heating rates from 5 to 60 K min^{-1}

Fig. 1 confirmed that ΔH_1 should be related to the quantity of the quenched-in amorphous phase or, alternatively, inversely proportional to the density of the crystalline grains embedded in the amorphous phase in each specific sample.

Discussion

Following theoretically the particular equilibrium binary [7] or eventual ternary [8] Ti–Zr–Ni phase diagrams, an endothermic peak should represent any reversible phase transformation like the melting or an α/β diffusionless Martensitic phase transition, which are not the nucleation-growth effects, in the heating regime; therefore, such endotherm should not have any kinetics. Thus, the temperature of its onset, T_x, being the main thermodynamic characteristics of each transformation, should be independent of the heating rate. However, because the width of each peak increases increasing the heating rate, thus also the temperature of this peak's maximum (T_p) should increase, the effect being related to the quantity of the evolved transformation heat has no transformation kinetics. Thus also the quantity E^*_{endo}, notwithstanding that it was possible to deduce technically its value by the Kissinger method [5], as shown in Table 1, is principally false.

Consequently, we suppose that the onset temperature of our endothermic peak $T_{x\mathrm{endo}}$ does not shift with increasing Φ; however, the temperatures of the exothermic peaks R2′ and R2″, being thermally activated phase transformations, increase. For the reason that both R′ and R″ peaks significantly overlap with the "non-kinetic" Rendo peak, probably the positions of their minima, namely the temperatures $T_{p2'}$ and $T_{p2''}$ need not to be the true minima and thus corresponding values of activation energies of R2′ and R2″ effects, namely $E^*_{2'}$ and $E^*_{2''}$ need not represent the true values of the activation energies (see $E^*_{2'}$ for the sample M1521 in Table 1).

In addition, analyzing the shape of the peaks R2′ and R2″ and Rendo, we suppose that the reactions R2′ and R2″ represent the same effect. This exotherm (being R2) should be superimposed by the endotherm Rendo. Such situation is supported by the measurements of the sample M1576 (Fig. 5), where, especially, no endothermic effect is present and accordingly only one clear authentic exothermic effect is manifested for all heating rates. Its activation energy is $E^*_2 = 331 \pm 18$ kJ mol^{-1}. This exothermic effect is relatively large. However, as the total exothermic reaction heat in the sample M1576 is $\Delta H_{\mathrm{total}} = -77$ J g^{-1}, the R2 exothermal effect $\Delta H_1 = -15.3$ J g^{-1} is only ∼20% of the total heat effect.

Following the DSC curves, the heat absorbed by the endothermic effect Rendo is much smaller. Assuming that the effects in all samples are same and only quantities of related phases vary, the sample M1522 presents no exotherm R2 and the clear effect Rendo recompenses hardly 5% from the total exothermic heat $\Delta H_{\mathrm{total}} = -131$ J g^{-1}, in this case (see Table 1). Even more, the R2 and Rendo effects might be mutually related. However, following our interpretation, we may assume that they are independent. Finally, the Rendo, being the endothermic effect, should be reversible. However, this is not entirely satisfied. Namely, eventually an other slightly smaller but wider endothermic effect Rendo2 (∼4–6 J g^{-1}) is registered in each following run (an equivalent measuring cycle immediately following the first one after quenching at −200 K min^{-1}). A typical sequence of the measured DSC curves for such $Ti_{45}Zr_{38}Ni_{17}$ ribbon which manifests the ample Rendo effect is seen in Fig. 6.

The summarization of the thermodynamic parameters, activation energies, and pre-exponential factors of all ribbons is given in Table 1 and Fig. 7. Our interpretation of

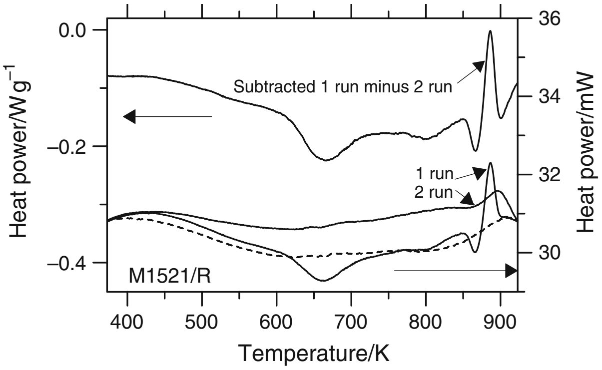

Fig. 6 The difference between the DSC curves of the as-prepared sample (1 run), the same sample pre-heated to 923 K (2 run) potentially being the baseline for the first measurement and the resulting (false) subtraction of such two curves. *Dashed line* is the measurement of the empty pan being the true baseline

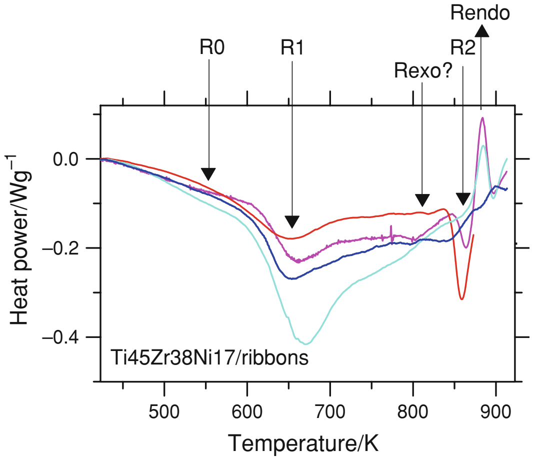

Fig. 7 The DSC curves of various castings of the ribbon Ti$_{45}$Zr$_{38}$Ni$_{17}$ at the heating rate 40 K min^{-1}. *Dark blue line* for M1520, *violet* for M1521, *light blue* for M1522, and *red* for M1576 samples. (Color figure online)

the individual transformation steps R0, R1, R2, and Rendo is based on the XRD and TEM results.

The structure of the sample M1576 by TEM and XRD is shown in Fig. 8 in as-quenched state and after isothermal annealing. The as-quenched state represents a duplex structure consisting of a high density of IQ in amorphous matrix which evolves into a mixture of TiZr–Ni intermetallics and Laves phases. This sample does not contain the β phase.

The structure of M1520, M1521, M1522 samples in as-quenched state consists of β phase in amorphous matrix; no presence of IQs has been observed. After annealing, the formation of IQ phase and TiZr–Ni intermetallics from the amorphous matrix is observed followed by the formation of the Laves phase C14 at the expense of the β phase (Figs. 1 and 9).

The interpretation of the DSC effects correlated with the microstructure evolution is presented below.

The R0 transformation step has already been studied and characterized in details in [1], where the structural relaxation of the amorphous matrix and the formation of specific $\beta/\omega_{\mathrm{iso}}$ particles within the β phase have been identified. In our sample, M1576 neither the β phase in the as-quenched state nor the R0 exothermal affects during the heating exist. Therefore, we briefly conclude that the major thermal contribution to the R0 transformation step gives the β to ω_{iso} transformation.

R1 is the formation and growth of nanocrystalline spherulitic IQs from amorphous matrix—devitrification in the set of samples M1520–M1522. However, for the M1576, it reflects the growth of the already present IQs only. This explains the different values of the enthalpies and activation energies. It has already been shown that the nano-crystallization of amorphous metallic alloys follows either the Johnson–Mehl–Avrami kinetic equation (JMA) or the normal-grain-growth one (GG) [9, 10]. Thus, in the case of the JMA kinetics, E_1^* should represent just the

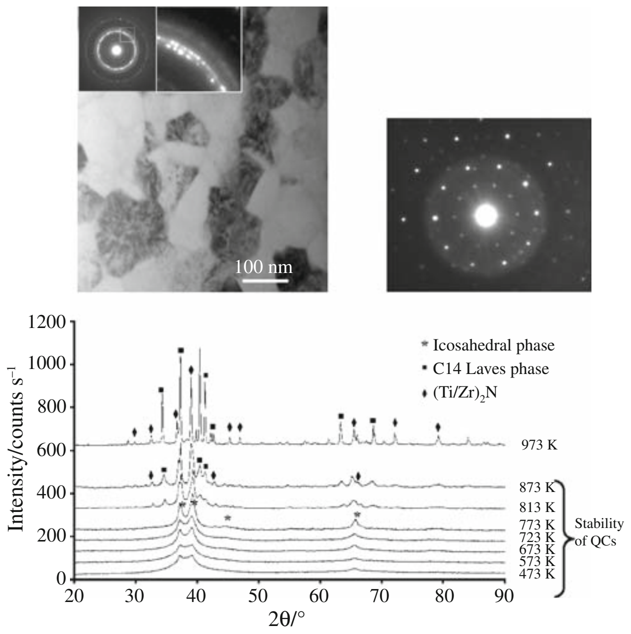

Fig. 8 TEM and selected area electron diffraction analyses of the M1576 ribbon in as-quenched state [4] and XRD after isothermal heat treatments for 30 min; the temperature of annealing is a parameter in the figure together with the phases identified

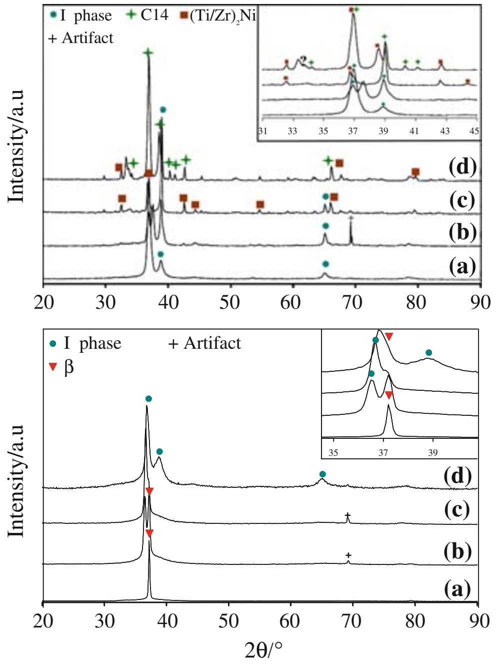

Fig. 9 XRD of M1520 in as-quenched state and after annealing for 30 min at selected temperatures (573, 623, 723, 773, 823, 923, and 1023 K) showing the subsequent formation of different phases

three-dimensional growth of the already present IQ nuclei or small IQ grains in the sample M1576, namely

$$E_1^* = E_G^*.$$

However, E_1^* should appertain to the weighted activation energy for the simultaneous homogeneous nucleation (E_n^*) and three dimensional growth (E_G^*) of the grains of the same IQ phase, namely

$$E_1^* = \left(E_n^* + 3E_G^*\right)/4$$

in the other samples. This interpretation is supported by the data in Table 1, where E_1^* for the sample M1521 equals to E_1^* for the sample M1522, and is substantially larger than E_1^* for the sample M1576. At present, only few quasi-crystals have been really observed and no results concerning the kinetics of the formation of the quasi-crystals have been known. Firstly, the hypothesis of the JMA kinetics and also the equivalence in the amorphous matrices of the analyzed samples should be proven, only then the absolute values of the apparent activation energies and pre-exponential factors might be interpreted. To justify the anomalously low, yet relatively precisely calculated E_1^* for the sample M1520, an eventual principal modification of the expected cluster-like structural units existing in the melt prior to its quenching might be taken into account due to exceeding of some critical temperature of the melt [11].

R2 in M1576 represents most probably the formation of intermetallic compounds and of the Laves phase. Neither the DSC nor the XRD data allow yet distinguishing with full confidence whether R2 is a simple single-step reaction or two-step transformation (R2 + Rexo?) in this case. The remaining samples form unambiguously (Fig. 9, XRD patterns at 923 and 1023 K) the intermetallic phases at lower temperatures. This may be considered as evidence of the true existence of the Rexo? reaction step which is vaguely indicated in the DSC traces (Fig. 2). The diversity of R2 and Rexo? transformation steps might be generalized for all $Ti_{45}Zr_{38}Ni_{17}$ ribbons. Because, the R2 exotherm is a well-defined simple peak in the case of M1576, its activation energy E_2^*, being assigned as $E_{2'}^* = 331$ kJ mol^{-1} in Table 1, thus should characterize the activation energy for the mentioned formation of Laves phase.

A question arises as to the nature of the Rendo reaction step. The sample M1576 exhibits no presence of the β phase neither it shows the presence of Rendo. This is what makes the sample M1576 different from all remaining ones where the presence of the β phase is without doubt. Thus, it might seem that the Rendo step corresponds to the α/β transformation. This effect is reversible and seen well in the second and subsequent DSC runs (see the DSC traces in Fig. 6 runs 1 and 2 for the sample M1521). Moreover, it lies in the vicinity of the temperature region in the phase diagrams where the reversible α/β structural transformation is expected. However, we have yet no proof of the existence of either α or β phase at the temperatures of the Rendo step.

More details related to the sample M1520 and its structural and kinetic evolutions are a subject of further studies.

Conclusions

Modifying the solidification rate (namely the melt temperature before the quench), qualitatively different ribbons of the same alloy $Ti_{45}Zr_{38}Ni_{17}$ can be produced. Comparison of their as-quenched microstructures reveals the competition between IQ and β-Ti(Zr) phases, both dispersed in an amorphous matrix. In the case of the high solidification rate, the as-quenched ribbons consist only of the A + β composite. Decreasing the solidification rate increases the quantity of the β particles. If the solidification rate is not high enough, the as-quenched ribbon consists only of the A + IQ composite. A typical DSC curve of the $Ti_{45}Zr_{38}Ni_{17}$ ribbon shows four distinct irreversible exothermic events: namely, the R0 exothermic pre-peak (being the relaxation of the amorphous matrix and also ω_{iso} precipitation from the β particles, if they are quenched-in), the R1 exotherm (being the devitrification, i.e., the precipitation of the IQs directly from the amorphous matrix, when the amorphous phase completely disappears), the Rexo? exotherm (the additional growth of IQs and the precipitation of $(Ti/Zr)_2Ni$ intermetallic phase), and upon heating to higher temperatures, the R2 exotherm (the formation of the Laves phase from IQs). At higher temperatures, the metastable β/ωiso particles gradually disappear also forming the more stable hexagonal compact α solid solution. However, then above 870 K, the low-temperature α solution reversibly transforms again to the high-temperature β solution; this α/β phase transition presents an endothermic peak Rendo in the continuous heating DSC curve.

Acknowledgements The authors gratefully acknowledge the financial support of the Slovak grant agencies under the contracts VEGA 2/0157/08, APVV-0413-06, and APVV-0102-07, project in the Framework COST P17 Action and the SAS Centre of Excellence "Nanosmart". H.L. is grateful to the SMATEC company (Belgium) for providing her doctorate scholarship.

References

1. Stroud RM, Viano AM, Gibbons PC, Kelton KF, Misture ST. Stable Ti-based quasicrystal offers prospect for improved hydrogen storage. Appl Phys Lett. 1996;69:2998–3000.
2. Qiang JB, Wang YM, Wang DH, Kramer M, Thiel P, Dong C. Quasicrystals in the Ti-Zr-Ni alloy system. J Non-Cryst Solids. 2004;334–335:223–7.

3. Lefaix H, Vermaut P, Janičkovič D, Švec P, Gloriant T, Portier R, et al. Unusual devitrification behaviour in rapidly solidified $Ti_{45}Zr_{38}Ni_{17}$ alloy. J Alloys Compd. 2008;460:392–9.
4. Lefaix H, Vermaut P, Janickovic D, Svec P, Portier R, Prima F. Processing and characterization of rapidly quenched Ti-based alloys: Influence of solidification rate on the as-quenched structures. J Alloys Compd. 2008;483:168–72.
5. Kissinger HE. Reaction kinetics in differential thermal analysis. Anal Chem. 1957;29:1702–6.
6. Elder JP. The general applicability of the Kissinger equation in thermal analysis. J Thermal Anal. 1985;30:657–69.
7. Massalski TB, Okamoto H, Subramanian PR, Kacprzak L, editors. Binary alloy phase diagrams. 2nd ed. Materials Park, OH: ASM International; 1990.
8. Davies JP, Majzoub EH, Simmons JM, Kelton KF. Ternary phase diagram studies in Ti-Zr-Ni alloys. Mater Sci Eng. 2000;294–296:104–7.
9. Illeková E, Šesták J. Crystallization of metallic micro- and nanocrystalline glasses, chap. 14. In: Šesták J, Holeček M, Málek J, editors. Some thermodynamic, structural and behavioral aspects of materials accentuating non-crystalline states. OPS Nymburg; 2009. p. 308–26, ISBN 978-80-87269-06-0.
10. Illeková E. Kinetic characterization of nanocrystal formation in metallic glasses. In: Idzikowski B, Švec P, Miglierini M, editors. Properties and applications of nanocrystalline alloys from amorphous precursors. NATO Science Series II: Mathematics, physics and chemistry, vol. 184. Dordrecht: Kluwer Academic Publishers; 2005. p. 79–90.
11. Kristiakova K, Švec P. Origin of cluster and void structure in melt-quenched Fe-Co-B metallic glasses by positron annihilation at low temperatures. Phys Rev B. 2001;64:014204.